nature communications

Article

https://doi.org/10.1038/s41467-026-69544-4

Unconventional spin-intertwined charge density wave in magnetic phases of kagome metal $GdTi_3Bi_4$

Received: 18 June 2025

Accepted: 4 February 2026

Published online: 12 February 2026

Check for updates

Xianghe Han[1,2,7], Hui Chen[1,2,7] ✉, Zhongyi Cao[1,2,7], Jingwen Guo[3], Chuyi Tuo[4], Ming-Rui Li[4], Fucong Fei[3], Hengxin Tan[5], Jianfeng Guo[1,2], Yanhao Shi[1,2], Runnong Zhou[1,2], Ruwen Wang[1,2], Zhen Zhao[1,2], Haitao Yang[1,2], Fengqi Song[3], Hong Yao[4], Binghai Yan[5], Shiyu Zhu[1,2] ✉, Ziqiang Wang[6] ✉ & Hong-Jun Gao[1,2] ✉

The symmetry breaking density waves and their interplay with spin and charge are crucial for understanding the correlated electronic states in quantum materials. However, symmetry-breaking density waves involving simultaneous charge and spin modulations remain largely unexplored. Here, we report the unconventional spin-intertwined charge density wave in magnetic kagome metal $GdTi_3Bi_4$ by scanning tunneling spectroscopy. We observe a 3Q charge density wave that is incommensurate with the crystalline lattice in both periodicity and orientation and breaks all mirror and rotation symmetries. The CDW undergoes incommensurate-commensurate transitions in a magnetic field and 3Q-1Q transitions as a function of applied magnetic field and temperature. Remarkably, the quantum and thermal melting of the CDW exhibits a phase structure closely resembling the bulk magnetization phase diagram of $GdTi_3Bi_4$, which provides evidence for the observation and manipulation of spin-intertwined CDW as a bulk property. Our findings reveal the microscopic textures of the intricate magnetic phases with unconventional charge-spin coupling, and offer insights into a broad class of multi-components density wave formation in kagome and other correlated quantum materials.

Electronic density waves, characterized by periodic spatial modulations of charge[1,2], spin[3,4] or Cooper pair density[5,6] that break lattice translational symmetry[1], have become widespread phenomena of correlated states in quantum materials. Recently, unconventional density waves have been reported to exhibit additional symmetry breaking that gives rise to novel electronic phenomena such as smectic orders with simultaneous rotational symmetry breaking[7–10], chiral density waves that break all mirror symmetries[11–14], and non-magnetic current density waves that break time-reversal symmetry[15]. Typically, a density wave involves periodic modulations in a single quantum degree of freedom, such as spin or charge. Consequently, a fundamental motivation is to explore the simultaneous modulation of both charge and spin, which is dubbed a spin-intertwined charge density wave (SCDW). The charge modulation of SCDW can be detected via

[1]Beijing National Center for Condensed Matter Physics and Institute of Physics, Chinese Academy of Sciences, Beijing, PR China. [2]School of Physical Sciences, University of Chinese Academy of Sciences, Beijing, PR China. [3]National Laboratory of Solid State Microstructures, School of Physics, School of Materials Science and Intelligent Engineering, Collaborative Innovation Center of Advanced Microstructures, Nanjing University, Nanjing, China. [4]Institute for Advanced Study, Tsinghua University, Beijing, China. [5]Department of Condensed Matter Physics, Weizmann Institute of Science, Rehovot, Israel. [6]Department of Physics, Boston College, Chestnut Hill, MA, USA. [7]These authors contributed equally: Xianghe Han, Hui Chen, Zhongyi Cao.
✉e-mail: hchenn04@iphy.ac.cn; syzhu@iphy.ac.cn; wangzi@bc.edu; hjgao@iphy.ac.cn

https://doi.org/10.1038/s41467-026-69544-4

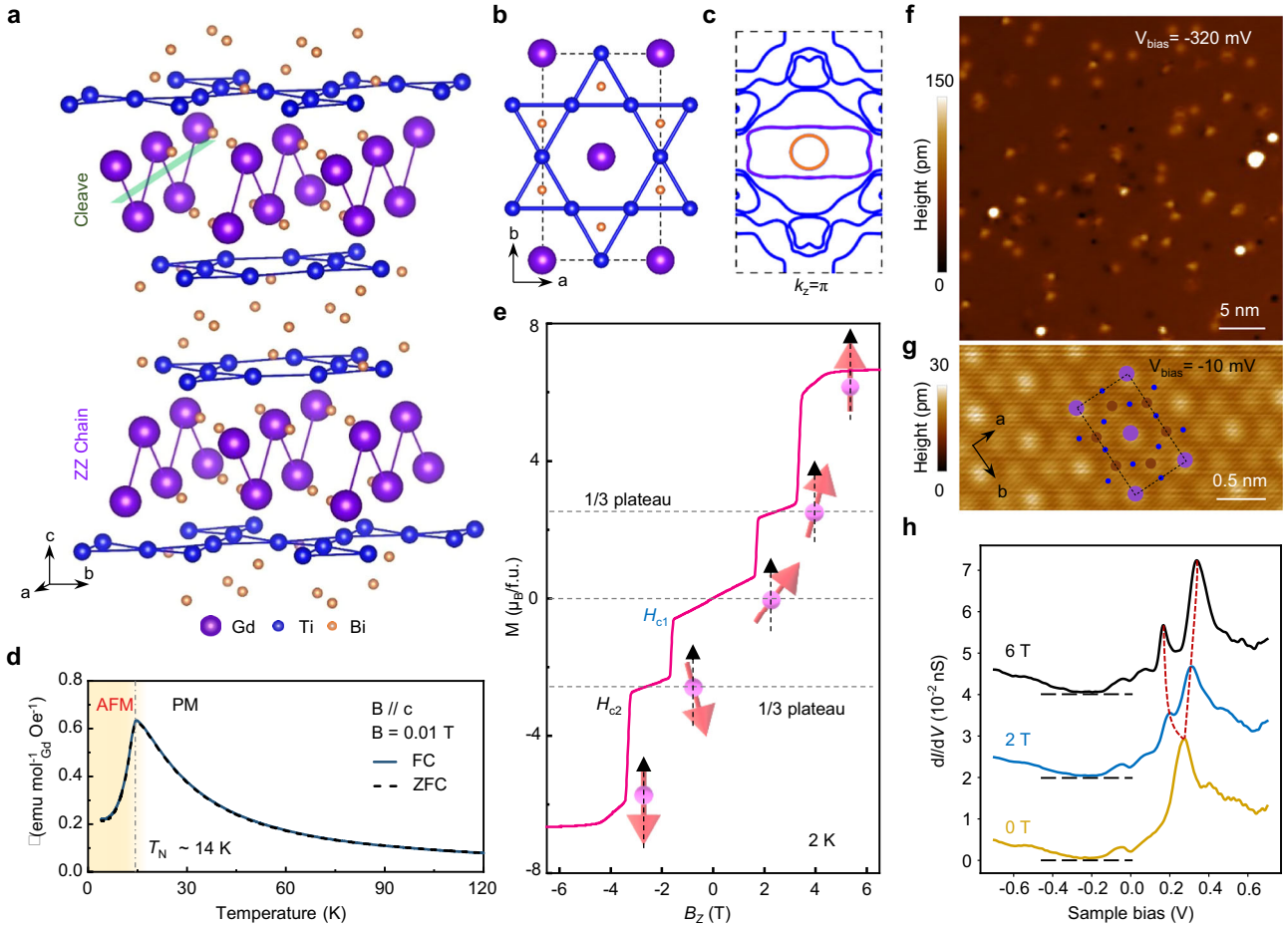

Fig. 1 | Structural, electronic, and magnetic properties of the $GdTi_3Bi_4$ crystal. **a** Atomic model of $GdTi_3Bi_4$ crystal, showing the bilayer kagome layer and Gd zigzag chain. Green shade indicates the cleaving plane. **b** Top view of the atomic model showing as-cleaved Gd surface with underlying kagome-lattice TiBi layer. **c** Calculated Fermi surface, showing contributions from the energy band of Gd zigzag chain (purple), Bi layer (orange) and Ti kagome layer (blue). **d** Temperature dependence of magnetization under a fixed magnetic field of 0.01 T, showing the antiferromagnetic transition occurs at T_N ~ 14 K (marked by the dashed dotted line). **e** Out-of-plane field dependence of magnetization, showing the two steps of magnetic transition with H_{c1} ~ 1.7 T and H_{c2} ~ 3.4 T. The arrows show a possible spin configuration on the Gd atoms. Relatively large-scale (**f**) and atomically resolved (**g**) STM images showing the Gd terminated surfaces with a quasi-hexagonal lattice. The atomic model is overlaid for clarification of Gd and Bi atoms. Tunneling parameter: (**f**), V_{set} = −320 mV, I_{set} = 450 pA (**g**), V_{set} = −10 mV, I_{set} = 100 pA. **h** The magnetic field dependent d*I*/d*V* spectra on Gd atom, showing a magnetic state at about 0.27 eV above E_F. V_{set} = 700 mV, I_{set} = 1 nA, V_{mod} = 2.5 mV. The red dashed line marks the splitting of the peak around 0.27 eV.

scanning probe microscope[16], while its spin content allows the tunability by an external magnetic field[17]. The SCDW has been proposed theoretically in the study of density waves on frustrated lattices[18]. However, up to date, the SCDW in the frustrated-lattice materials has rarely been observed.

Magnetic kagome metals have recently emerged as an ideal platform for investigating the interplay between the spin and charge degrees of freedom. Electronic density waves, which play a crucial role in the emergence of unconventional superconductivity[6,19,20], have been proposed for the magnetic kagome metals[21–23]. An intriguing example is that in the magnetic kagome metal FeGe, a charge density wave (CDW) emerges at temperatures below the magnetic transition, but the ordered magnetic moment exhibits a sudden change at the CDW transition, indicating a strong coupling between the magnetism and CDW[24,25]. Recently, the *RE*Ti_3Bi_4 (*RE*=rare earth metals) family exhibits unique fractional magnetization plateaus and topological band structure[26–30], making it a compelling candidate for studying the coupling between magnetic order and density wave formation, including the possibility of realizing unconventional charge-spin coupled states.

Here, we investigate $GdTi_3Bi_4$ using low-temperature scanning tunneling microscopy/spectroscopy (STM/STS) equipped with external magnetic field capability. We observe a three-component (3Q) CDW at the Gd-terminated surface in the magnetic ground state. By comparing the CDW and crystalline vectors, we show that the CDW is incommensurate with the crystalline lattice in both periodicity and orientation. In addition, the CDW is highly unconventional as it breaks all mirror and rotation symmetries, in addition to breaking translation symmetry. Remarkably, the CDW is highly manipulable by external magnetic fields, demonstrating its spin-charge coupled nature and providing evidence of spin-intertwined CDW. We further study the quantum and thermal melting phase diagram of the CDW in magnetic fields as a function of temperature, which reflects similar trends to the magnetization phase diagram of bulk $GdTi_3Bi_4$, providing compelling evidence for an intertwined spin-charge ordered state.

Results

$GdTi_3Bi_4$ has a layered orthorhombic lattice structure in the space group Fmmm (Fig. 1a). The prototype structure consists of four slightly distorted Ti kagome-lattice layers per unit cell, which is larger than that of kagome superconductor CsV_3Sb_5[31]. Another interesting structural motif of interest is the formation of Gd-Gd zigzag chains along *a* direction (Fig. 1a). The weak interlayer interactions between adjacent

Gd/Bi layers (light green shade in Fig. 1a) result in the Gd terminated surface (Fig. 1b) after cleaving the $GdTi_3Bi_4$ crystal[32]. The $GdTi_3Bi_4$ crystal exhibits quasi-two-dimensional energy band. The Fermi surface contains three pairs of bands (Fig. 1c): triangular bands from Ti 3*d* orbitals (blue), quasi-1D band from Gd 5*d* orbitals (purple), and an inner band from Bi 6*p* orbitals (orange). The hybridization of the Gd-Gd zigzag chain with Bi 6*p* orbital band results in the elongated shape of the inner pocket. The uniaxial direction of the ellipse is perpendicular to quasi-1D band.

The $GdTi_3Bi_4$ exhibits an antiferromagnetic ground state below a Néel temperature of T_N ~ 14 K, as demonstrated by magnetization measurements at a temperature range from 2 K to 120 K (Fig. 1d). In addition, $GdTi_3Bi_4$ shows a specific 1/3 plateau state with the magnetic field along the *c*-axis between H_{c1} and H_{c2}. When the field is higher than H_{c2}, it turns to fully polarized ferromagnetic states (Fig. 1e).

We first study the electronic states of $GdTi_3Bi_4$ at atomic scale. The STM image of Gd terminated surfaces show flat terrace with randomly distributed defects (Fig. 1f). The height difference between two adjacent terraces is about 1.3 nm, consistent with half of the lattice constant of 1.3 nm along *c* direction (Fig. S1). The typical atomically-resolved STM images at relatively large sample bias, e.g., 320 mV, show hexagonal lattice with Gd atoms as Gd layer is slightly higher than the Bi atomic layer (Figs. 1f and S2). When approaching the tip closer to the sample surface by using small sample bias e.g., −10 mV, the STM images resolve both Gd and Bi atoms (Fig. 1g, for details see Fig. S2). The local density of states (LDOS) at Gd terminated surface display a V-shape metallic feature around the Fermi level (E_F) with a broad conductance peak at 270 mV, as evidenced by the spatially averaged d*I*/d*V* spectra (Fig. 1h). The broad peak is spatially localized at the Gd atoms, as evidenced by the spatial distribution of d*I*/d*V* spectra (Fig. S3). In addition, the broad peak gradually split with increasing external magnetic field perpendicular to the sample surface (Fig. 1h, for details see Fig. S4). Thus, we attribute the broad peak to a localized magnetic state from Gd atoms.

In addition to the local magnetic state at 270 meV, there are some electronic states at low energies in the d*I*/d*V* spectra of Gd surface. The spatial distribution of LDOS around E_F e.g., 20 meV (Fig. 2a), shows the real-space LDOS oscillation around the defects originated from quasiparticle interferences (QPI). These QPI signals result in an elongated circular pattern centered at Γ point in the corresponding Fourier transform (FT) image of d*I*/d*V* map (Fig. 2b). The elongated circular QPI is originated from the intra-band scattering of ellipse band. The long axis of such QPI pattern corresponds to the uniaxial direction of the ellipse band from Bi band. By comparing the chain direction with the calculated Fermi surface, we attribute the long axis of elongated circular QPI pattern ($\boldsymbol{Q}_B^3$ in Fig. 2b) to the zigzag chain direction (*a* direction).

The FT cut along one direction (orange dashed line in Fig. 2b) in the *q* space shows a dispersing parabolic curve (white dashed dotted curve in Fig. 2c), corresponding to the expending elongated circular QPI patterns which grows outwards with increasing energy (details see Fig. S5). The dispersive parabolic band is interrupted by the localized magnetic state at an energy of 270 meV. Such interruption is attributed to the hybridization between itinerant electrons and local moments from Gd atoms[33,34].

We then focus on the itinerant electronic states near E_F. In the FT of both STM topography (Fig. 2d, e) and low-energy d*I*/d*V* maps (Fig. 2f, g), there are three pairs of additional peaks around the circular QPI pattern (For details, see Fig. S6). To understand the origin of these extra peaks in the FT, we collect the d*I*/d*V* maps at various energies, i.e., $g(\boldsymbol{r}, E)$ ($\boldsymbol{r}$ is the real space location while E is the energies). The $g(\boldsymbol{r}, E)$ maps in large energies (e.g., −280 meV, Fig. 2f) show super-modulations propagating along three directions, forming a superlattice over the pristine structural lattice of Gd atoms (Fig. 2h). These additional modulation gives rise to the additional peak structures seen in the FTs, termed as $\boldsymbol{q}^i$ ($i = 1, 2, 3$) vectors (Fig. 2g).

To distinguish signals between dispersive QPI and non-dispersive CDW orders, we study the energy dependence of the $\boldsymbol{q}^i$ vectors associated with the peaks in the FT. To do this, we obtain linecuts from FTs of the LDOS maps along the three directions in momentum space and plot this as a function of energy (Fig. 2i). Contrary to energy-dispersive features such as QPIs, we find that the magnitudes of these three $\boldsymbol{q}$ vectors show no energy dependence (details see Fig. S7). This indicates that the observed modulations arise from a CDW order in this material. We label the CDW vectors $\boldsymbol{q}^i_{CDW}$ by the blue ($\boldsymbol{q}_1$), red ($\boldsymbol{q}_2$), and green ($\boldsymbol{q}_3$) squares. The periodicities of the CDW in three directions are close to but not equal to three times of the lattice constant a_0 (the vector length: $|\boldsymbol{q}^1_{CDW}|=0.31|\boldsymbol{Q}^1_B|$,$|\boldsymbol{q}^2_{CDW}|=0.37|\boldsymbol{Q}^2_B|$ and $|\boldsymbol{q}^3_{CDW}|=0.40|\boldsymbol{Q}^3_B|$).

The 3Q CDW is incommensurate with the lattice periodicity. In addition, the three CDW vectors do not align with crystalline lattice directions precisely (cyan lines in Fig. 2g). This leads to distorted hexagonal unit cell of the CDW (Fig. 3a) that breaks rotation and all mirror symmetries, indicating that the CDW is chiral[11]. We stress that the intensities of the CDW components, which are reflected in the heights of the CDW peaks in the FT images, are generally different in different directions and difficult to characterize systematically in our measurements. Thus, we will not comment specifically on the rotation symmetry and rotation symmetry breaking reflected by the CDW intensity in the conductance maps. Instead, we focus on the symmetry properties of the CDW defined by the wavevectors $\boldsymbol{q}^i$, i.e., the CDW peak locations in the FT images. To reveal the spatial configuration of the CDW, we filter the FT images by passing $\boldsymbol{q}^i_{CDW}$ and $\boldsymbol{Q}^i_B$ spots and produce the real space image by the inverse FT (Fig. 3b), which highlights that the CDW is incommensurate with both the periodicity and orientation of the underlying lattice.

The incommensurate CDW with chirality is tunable by the external magnetic field. We study the evolution of three CDW vectors with the external magnetic field perpendicular to the sample surface (B_z) at 0.4 K. In the magnetic ground state ($B_z < \mu H_1$), the 3Q CDW remain approximately unchanged (Fig. 3c). In contrast, increasing the field to the 1/3 plateau state ($\mu H_1 < B_z < \mu H_2$), the three CDW vectors jump quickly to align with the crystalline directions. Independent with the magnetic field, the three $\boldsymbol{q}^i_{CDW}$ vectors satisfy the triangle relationship $\boldsymbol{q}^1_{CDW} + \boldsymbol{q}^2_{CDW} + \boldsymbol{q}^3_{CDW} = 0$, (Fig. S9). Further increasing B_z, the $\boldsymbol{q}^3_{CDW}$ vector first disappears as the CDW gradually melts and all the CDW peaks become invisible in the FM state when $B_z > \mu H_2$ (Fig. 3c), indicating the complete quantum melting of the CDW in the fully polarized ferromagnetic phase. It suggests the strong coupling of quantum mechanical ground state of CDW to the magnetic ordering.

We note the 3Q CDW order in the 1/3 plateau magnetization phase, e.g., at 2.25 T, shows restored rotation and all mirror symmetries in terms of both vector orientation and magnitude, forming a nearly commensurate $3a_0 \times 3a_0$ CDW pattern (Fig. 3d). In addition, the inverse FT image obtained by filtering out $\boldsymbol{q}^i_{CDW}$ and $\boldsymbol{Q}^i_B$ spots reveals real-space $3a_0 \times 3a_0$ modulations that are nearly commensurate with the underlying crystalline lattice (Fig. 3e).

To demonstrate the robustness and repeatability of the field-induced switching of 3Q CDW between ground state and 1/3 plateau state, we systematically study the CDW under the sequence of magnetic field of (−2.25 T)-0 T-(2.25 T) (Fig. 3f, g). We quantitively study the variation of 3Q CDW with external magnetic field by defining the relative angle and relative length. The relative angle is the angle difference between the CDW vectors and corresponding Bragg vectors. The positive (negative) value means the CDW vector is on the right (left) of the closest Bragg vector. The three relative angles transform from finite values to zero when B_z increase to μH_{c1} (Fig. 3f). The values of the three relative lengths ($|\boldsymbol{q}^i_{CDW}|/|\boldsymbol{Q}^i_B|$) deviate from 1/3 at 0 T and approach to 1/3 when B_z increases to μH_1 (Fig. 3g). Reversing the filed direction, we observe similar transitions in both relative angle and

https://doi.org/10.1038/s41467-026-69544-4

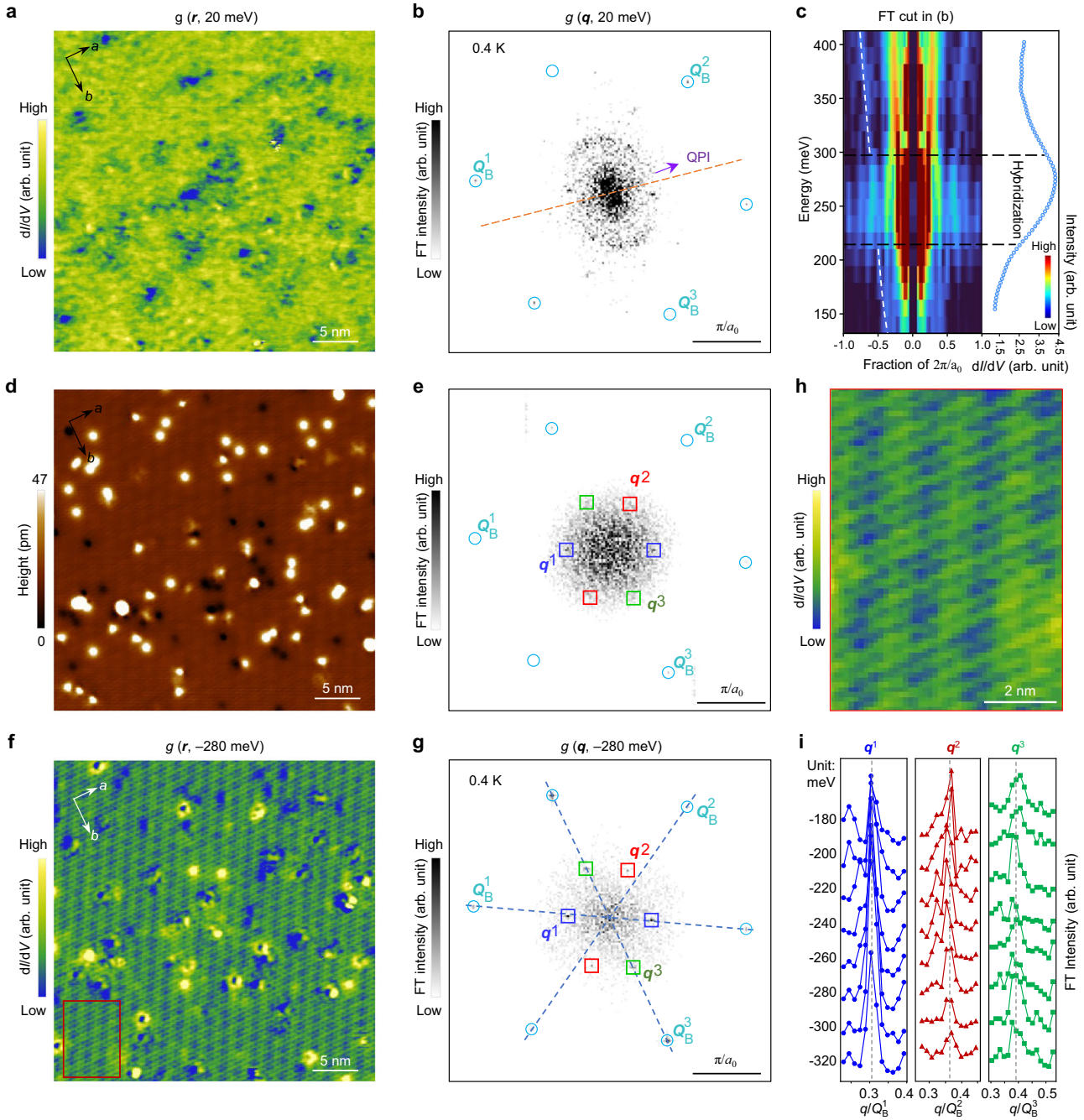

Fig. 2 | Spectroscopic imaging of the quasiparticle interference pattern and 3Q CDW at the surface of $GdTi_3Bi_4$ crystal. The d*I*/d*V* map at 20 meV, $g(\boldsymbol{r}, 20\ \text{meV})$ (**a**) and corresponding FT, $g(\boldsymbol{q}, 20\ \text{meV})$ (**b**), showing elongated circular QPI patterns (marked by the purple arrow in (**b**)) around impurities. $V_{set} = 20$ mV, $I_{set} = 200$ pA, $V_{mod} = 3$ mV. **c** FT cut of $g(E, \boldsymbol{q})$ along the orange dashed line in (**b**) as a function of energy, showing the electron-band-like dispersion (highlighted by the white dashed lines) of the circular QPI patterns is interrupted around 270 meV (left panel). The energy range of interruption corresponds to the magnetic local bound states at 270 meV as indicated by the d*I*/d*V* spectrum at Gd surfaces (right panel, highlighted by black dashed lines). The topography of Gd terminated surface (**d**) and corresponding FT (**e**), showing the emergence of density waves (marked by squares in different colors). $V_{set} = 1000$ mV, $I_{set} = 500$ pA. The $g(\boldsymbol{r}, -280\ \text{meV})$ (**f**) and $g(\boldsymbol{q}, -280\ \text{meV})$ (**g**), showing three pairs of density wave peaks ($\boldsymbol{q}^i$, marked by squares in different colors). $V_{set} = -280$ mV, $I_{set} = 450$ pA, $V_{mod} = 7$ mV. The dashed blue lines in (**g**) mark the direction of Q_B-Q_B. **h** Zoom-in of the region marked by red rectangle in (**f**), showing the superlattice corresponding to the three pairs of density wave peaks. **i** Linecuts in Fourier space along the three directions of $\boldsymbol{q}^i$. The positions of $\boldsymbol{q}^i$ do not change in a large energy range from −180 to −320 meV, consistent with the formation of CDW order.

length with weak hysteretic behaviors (Fig. S10). Therefore, the incommensurate CDW in the AFM ground state evolves into a nearly commensurate $3a_0 \times 3a_0$ CDW in the 1/3 plateau state.

Having studied the quantum melting at low temperature by the magnetic field[35], we turn to investigate the thermal melting[36] of the 3Q CDW by increasing the temperature in zero magnetic field. We measure and compare the FTs of d*I*/d*V* maps at various temperatures over an identical surface region (Fig. 4a). When the temperature is increased from 0.4 K, the three CDW peaks remain stable at 2.0 K. However, in the temperature range from 2.2 K to 2.6 K, we observe that the intensities of two CDW peaks ($\boldsymbol{q}^2$ and $\boldsymbol{q}^3$) diminish sequentially (see method and Fig. S12). At 4.2 K, only a unidirectional 1Q-CDW order

https://doi.org/10.1038/s41467-026-69544-4

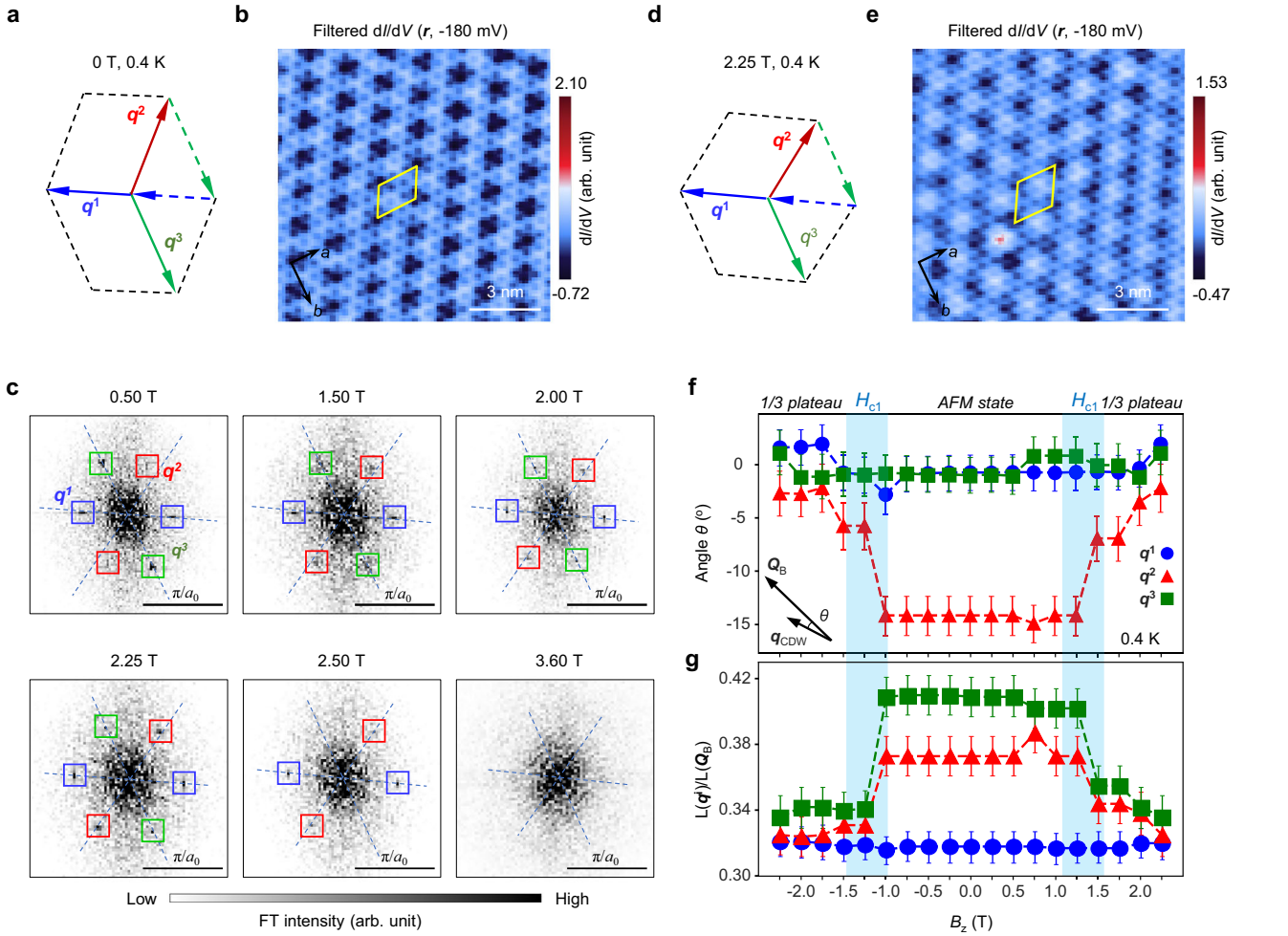

Fig. 3 | Manipulation of 3Q CDW by the magnetic field perpendicular to the surface of $GdTi_3Bi_4$ crystal. a Schematic of three density wave vectors $\boldsymbol{q}^i_{CDW}$ at 0 T (marked by arrows in different colors), showing that the distorted hexagonal unit cell of the CDW break rotation and all mirror symmetries in the q space. **b** The filtered d*I*/d*V* maps by passing the $\boldsymbol{q}_{CDW}$ and $\boldsymbol{Q}_B$ in the FT images, showing that the CDW is incommensurate with crystalline lattice in both periodicity and orientation in the real space. The yellow parallelogram highlights the unit cell of the CDW. For the unprocessed data, see Fig. S8. **c** Zoom-in FTs of d*I*/d*V* maps, g(180 meV, $\boldsymbol{q}$) at a perpendicular magnetic field (B_z) of 0.5, 1.5, 2.0, 2.25, 2.5, and 3.6 T, respectively, showing that three CDW vectors vary with increasing B_z. The dashed blue lines mark the direction of Q_B-Q_B, highlighting the orientation differences between Bragg peaks ($\boldsymbol{Q}^i_B$) and density wave peaks ($\boldsymbol{q}^i_{CDW}$). For the **d***I*/d*V* maps, see Fig. S10. **d** Schematic of three density wave vectors $\boldsymbol{q}^i_{CDW}$ at 2.25 T, showing that the hexagonal CDW unit cell exhibits rotation and mirror symmetries in the q space, which is termed as nearly commensurate $3a_0\times3a_0$ CDW (marked by arrows in different colors). **e** The filtered d*I*/d*V* maps after passing the $\boldsymbol{q}_{CDW}$ and $\boldsymbol{Q}_B$ spots in the FT images at 2.25 T, showing the nearly commensurate $3a_0\times3a_0$ CDW in the real space. The yellow rhombus highlights the unit cell of the CDW. For the unprocessed data, see Fig. S8. plots of orientation angle differences (**f**) and relative length (**g**) with increasing B_z, showing the field induced incommensurate-commensurate transition of CDW order. The background light blue shade indicates the critical field H_{c1}. The error bars in (**f**) and (**g**) are defined in Fig. S11. For all d*I*/d*V* data in this Figure, V_{set} = −180 mV, I_{set} = 450 pA, V_{mod} = 8 mV.

described by the single vector $\boldsymbol{q}^1$ is observed (Fig. 4a). Further increasing the temperature, the intensity of $\boldsymbol{q}^1$ diminishes and disappear at approximately the Néel temperature (T_N ~ 14 K). The closeness of the melting temperature of 1Q-CDW T_{CDW} to the Néel temperature T_N indicates that the thermal melting of CDW is accompanied by that of the magnetic order, suggesting that the CDW is intertwined with magnetism thermodynamically.

It is instructive to investigate the magnetic field dependence of the 1Q-CDW phase. When the field is increased to above 1 T, the 1Q CDW transitions into another nearly commensurate 3Q CDW state (Fig. 4b, c). The latter is then gradually suppressed when the magnetic field is increased to 3.4 T. (Fig. S14). The field-induced melting at 4.2 K is smaller than the value at 0.4 K, indicating the importance of the underlying thermal fluctuations at reducing the ordered magnetic moment.

The phase diagram for the observed cascades of density wave in the plane of temperature and magnetic field is constructed using the STM data taken at the phase locations marked by the red symbols (Fig. 4d, for details see Fig. S10, S13 and S14). For comparison, we also present the magnetic phase diagram determined recently by bulk magnetization and magnetic force microscopy measurements (Fig. 4e, details see method part and Fig. S16, S17). The two phase diagrams (Fig. 4d, 4e) show a remarkable similarity in the overall structure of phase regions with approximate alignment of the phase boundaries. The magnetic ground state (AFM-I in Fig. 4e) has AFM order with the magnetic moments in a–c plane without b component[37]. The corresponding ground state observed by STM (orange region in Fig. 4d) is an incommensurate 3Q charge density wave. Increasing the magnetic field, the magnetic ground state undergoes a hysteretic transition to the phase with 1/3 magnetization plateau and magnetic moments still confined to the a–c plane (1/3-plateau-I in Fig. 4e). Intriguingly, this field-induced magnetic transition is captured in the density wave phase diagram by the field induced, weakly hysteretic incommensurate to nearly commensurate 3Q CDW transition in Fig. 4d (and Figs. 3f,

https://doi.org/10.1038/s41467-026-69544-4

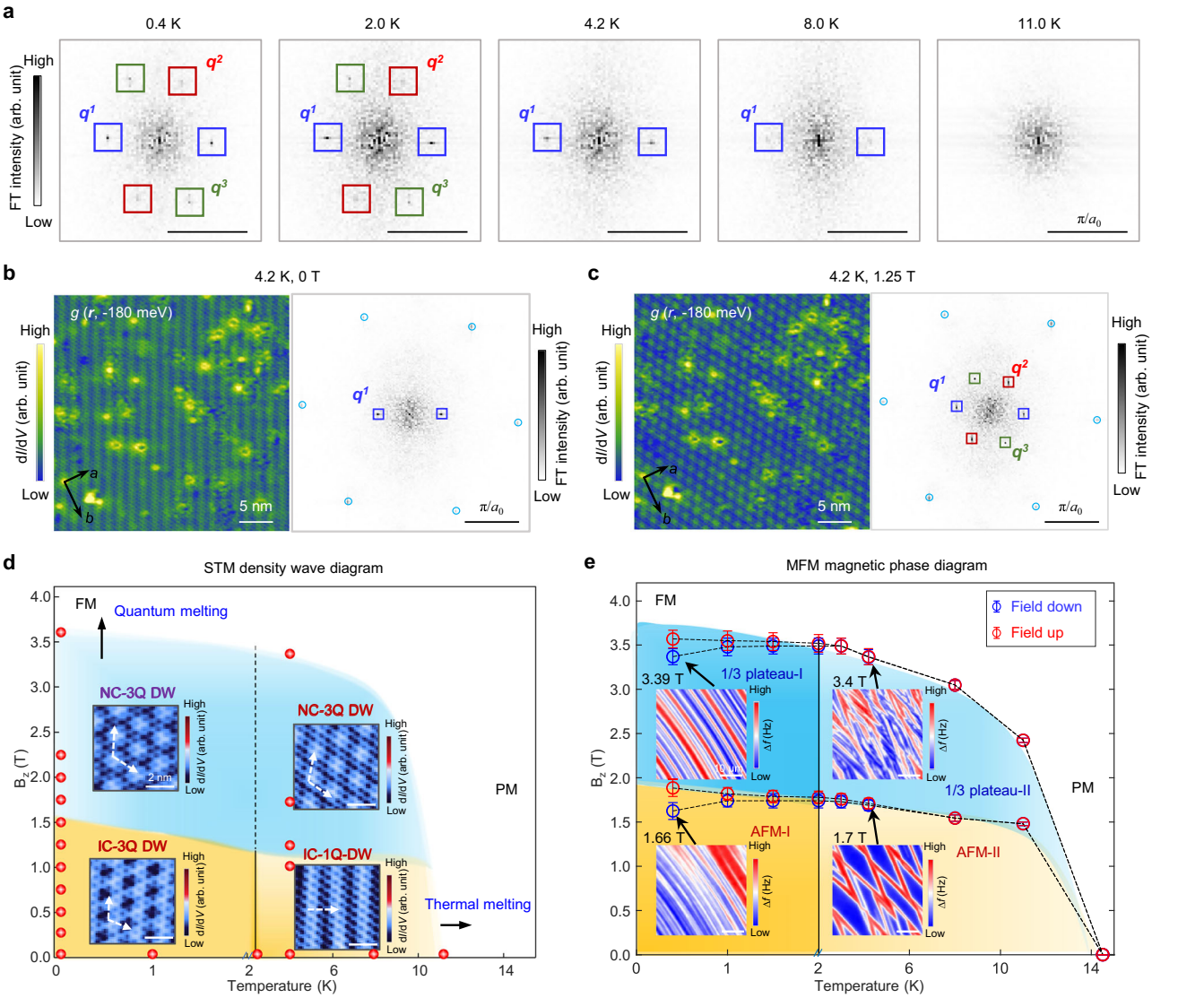

Fig. 4 | Temperature evolution and field-temperature phase diagram of spin-intertwined charge density wave in $GdTi_3Bi_4$. a Zoom-in FTs of d*I*/d*V* maps at temperatures of 0.4 K, 2.0 K, 4.2 K, 8.0 K, and 11.0 K, respectively, showing the 3Q-1Q CDW transition across 2 K and thermal melting near T_N ~ 14 K. For the d*I*/d*V* maps, see Fig. S13. The d*I*/d*V* maps at −180 mV and corresponding FTs at a temperature of 4 K and a B_z of 0 T (**b**) and 1.25 T (**c**), showing the transition from 1Q density wave at 0 T to 3Q density wave at 1.25 T. The CDW peaks are marked by squares in different colors. Tunneling parameter: (**b**), V_{set} = −150 mV, I_{set} = 450 pA, V_{mod} = 8 mV. **c** V_{set} = −150 mV, I_{set} = 500 pA, V_{mod} = 8 mV. Approximate temperature vs magnetic field schematic phase diagram of density wave from STM measurements (**d**), which shows strong correlation with the magnetic phase diagram based on the MFM measurements (**e**). DW density wave, AFM antiferromagnetic state, FM ferromagnetic state, PM paramagnetic state. The difference between phase I and phase II is that the ***b*** component of the magnetic moment is absent in phase I but present in phase II. The data shown in the four phases are MFM data measured in the same region. The domain contrast between data comes from magnetization difference between the four magnetic phases (for details, see Fig. S16 and S17). The red circles in (**d**) are experiments results measured by STM. The error bars in (**e**) correspond to the transition intervals.

g and S10). Similarly, increasing the temperature from the magnetic ground state drives a transition from AFM-I to the phase AFM-II characterized by a bifurcation in magnetic anisotropy that introduces a *b*-axis component to the magnetic moments[37] (Fig. 4e). This magnetic transition corresponds to the incommensurate 3Q CDW to an incommensurate 1Q CDW transition observed by STM (light yellow in Fig. 4d). Driving the latter by increasing magnetic field into the nearly commensurate 3Q CDW in Fig. 4d accompanies the field-induced transition from AFM-II to the 1/3 plateau-II phase (Fig. 4e).

Discussion

The consistence between CDW and MFM diagram demonstrates that the CDW observed by STM on the surface is a bulk property that reveals the microscopic textures of the intricated magnetic structure in bulk $GdTi_3Bi_4$ crystals. Notably, Although the Gd–Gd zigzag chains are disrupted upon cleavage, the surface atomic structure remains essentially identical to that of the bulk, with no indication of Gd reconstruction[38]. Considering the strong interlayer magnetic coupling, the observed CDW is reasonably attributed to the bulk state.

We next turn to discuss the possible origin of observed CDW. The observation of the cascades of CDW closely tracking the magnetic phases and transitions supports that the translation symmetry breaking involves both charge and spin in the primary modulations, giving rise to the possible formation of spin-intertwined CDW. To date, the magnetic structure of $GdTi_3Bi_4$ is not yet fully established, as direct experimental probes such as neutron scattering are lacking. However, recent studies using Magnetic Force Microscopy[37] proposed a possible magnetic structure with a period of approximately $3 \times a_0$ in real space

within the *ab* plane. This periodicity closely matches the CDW wave vector observed in our STM measurements. Therefore, we develop a Ginzburg-Landau (GL) model incorporating strongly coupled CDW and AFM order parameters (For details, see Section VI in the Supplementary information) to phenomenologically understand the observed phase diagram of CDW in $GdTi_3Bi_4$. The model's crucial feature is the strong coupling between spin and charge, which is microscopically justified by the Fermi surface nesting driving the AFM order, and the momentum conservation that links the AFM and CDW ordering vectors. The model also includes mutual competition between different AFM components, a consequence of their overlapping nesting regions on the Fermi surface (Fig. S18). This theoretical framework, driven by nesting-induced coupling and competition, successfully reproduces the key experimental observations: simultaneous onset of the CDW and AFM orders, and the overall topology of the complex temperature-magnetic field phase diagram (Fig. S19). It thus provides a concrete understanding of the intricate spin-charge interplay in $GdTi_3Bi_4$.

The possibility that the CDW is purely charge in nature but stabilized or modified by magnetic ordering is ruled out by the close correspondence between the CDW phase diagram and the complex magnetic behavior. In systems where magnetic order stabilizes the CDW (e.g., FeGe)[24], the magnetic transition typically occurs at a higher temperature than the CDW transition. In contrast, in $GdTi_3Bi_4$, the CDW transition temperature is nearly identical to the Néel temperature ($T_N \approx 14$ K), indicating a cooperative rather than hierarchical relationship. Furthermore, theoretical calculations reveal that the energy difference between the AFM-I and AFM-II states at zero field is too small[37] to account for the observed 3q-to-1q CDW transition if the CDW were merely stabilized by magnetism. These results suggest that the CDW is intrinsically coupled to spin degrees of freedom, consistent with a spin–intertwined charge density wave.

Indeed, a commensurate 1Q spin density wave (SDW) order has recently been detected by neutron scattering[30] in a related magnetic kagome compound $CeTi_3Bi_4$. It is natural to speculate that the SDW thus directly detectable by spin-polarized STM on the surface of $GdTi_3Bi_4$, which deserves further studied in the future[39]. By studying the spin-intertwined CDW order and its sequential quantum and thermal melting, we provide microscopic insights into the magnetic phases of magnetic kagome metals and establish a paradigm for STM enabled detection of magnetic phases and manipulation, offering potential applications in spintronics and the next-generation topological materials engineering.

Methods

Single crystal growth of $GdTi_3Bi_4$

The flux method is utilized to synthesize the high–quality single crystals. The starting elements of Gd: Ti: Bi in the molar ratio of 1.2: 1: 20 are mixed in an alumina crucible and sealed in a quartz ampule. The ampule is placed in a furnace and heated to 1000 °C at a rate of 1 °C/min. After maintaining it at 1000 °C for 16 h, the ampule is slowly cooled down to 520 °C in 2000 min. The hexagonal shaped single crystals are obtained after centrifuging in order to remove the excess flux[32].

Scanning tunneling microscopy/spectroscopy

The samples used in the STM/S experiments were cleaved at low temperature (80 K) and immediately transferred to an STM chamber and cooled down to 4.2 K. Experiments were performed in an ultra-high vacuum (1×10^{-10} mbar) ultra-low temperature STM system equipped with external magnetic field perpendicular to the sample surface. The lowest base temperature is 0.4 K with an electronic temperature of 650 mK (calibrated using a standard superconductor, Nb crystal). The magnetic field up to 11 T was applied using the zero-field cooling technique. All the scanning parameters (setpoint voltage V_s and tunneling current I_t) of the STM topographic images are listed in the figure captions. The d*I*/d*V* spectra were acquired by a standard lock-in amplifier at a modulation frequency of 973.1 Hz; the modulation bias (V_{mod}) is listed in the figure captions. Non-magnetic tungsten tips were fabricated via electrochemical etching and calibrated on a clean Au(111) surface prepared by repeated cycles of sputtering with argon ions and annealing at 500 °C. To remove the effects of small piezoelectric and thermal drifts during the acquisition of d*I*/d*V* maps, we apply the Lawler-Fujita drift-correction algorithm[40] in angle and relative length ($|\boldsymbol{q}^i_{CDW}|/|\boldsymbol{Q}^i_B|$) calculation in Fig. 3, which corrects the atomic Bragg peaks in the FTs of d*I*/d*V* maps to a single pixel to enhance calculational accuracy. The Fourier analyses in Figs. 2 and 4b, c are direct Fast Fourier transforms of corresponding real space signals. Figure 3b, e are inverse Fourier transforms of the filtered Fourier transforms. The methodological details are listed in the caption of Fig. S8.

Magnetic force microscopy

The MFM experiments were captured by a commercial magnetic force microscope (attoAFM, attocube) using a commercial magnetic tip (MFMR, Nanoword) based on a closed-cycle He cryostat (Bluefors) and dilution refrigerator system (Bluefors), combined with a vector magnet (9-3-1, Bluefors). The scanning probe system was operated at the resonance frequency of the magnetic tip, approximately 70 kHz. The MFM images were taken in constant height mode with the scanning plane nominally ~250 nm above the sample surface. The MFM signal, i.e., the resonance frequency shift (Δf), is proportional to the out-of-plane stray field gradient. Darker (brighter) magnetic contrast indicated the more attractive (repulsive) interaction between the magnetic tip and the sample stray field. $GdTi_3Bi_4$ single crystals were cleaved under ambient conditions to expose fresh surfaces before conducting MFM measurements.

Critical temperature of 3Q-1Q transition of 3Q CDW

To quantitatively evaluate the melting of the CDW phase, we extract FT linecuts from the center of the FT through each of the three CDW peaks as a function of temperature from 1.0 K to 2.6 K (details see Fig. S12). By plotting the peak intensities as a function of temperature, we find that the $\boldsymbol{q}^1$ peak keeps unchanged while the other two peaks get progressively suppressed with increasing temperature (Fig. S12). The critical temperature for $\boldsymbol{q}^3$ is 2.5 K, which is higher than that of $\boldsymbol{q}^2$ (2.2 K). The distinct critical temperature for the suppression of three CDW peaks further demonstrates the independent order parameters of the 3Q CDW orders. The critical temperature around 2.2 K corresponds to the magnetic state transition in the MFM measurements (Figs. 4e and S16 and S17), further supporting the strong correlation between the CDW and magnetic orders.

Magnetic transition at the critical temperature of ~2 K

We investigate the magnetic transition below 2 K by performing magnetic force microscopy (MFM) measurements of $GdTi_3Bi_4$ single crystals at temperatures. At 0.4 K, we observe the formation and evolution of uniformly stripe domains along the *a*-axis direction during the magnetic transition process due to the quasi-1D magnetic structure of $GdTi_3Bi_4$, leading to a pronounced in-plane magnetic anisotropy (Fig. S16). During the increasing magnetic field procedure, stripe domains emerge at 1.79 T and vanish completely at 1.99 T, indicating a magnetic transition within a range of 0.20 T. However, during the decreasing magnetic field procedure, the stripe domains reappear between 1.53 T and 1.73 T, suggesting a magnetic field hysteresis of 0.24 T (Fig. S16). In contrast, as the temperature increases to 4 K, the stripe domains on longer align strictly along the *a*-axis and exhibit some deviation (Fig. S17). Meanwhile, the hysteresis becomes negligible, and the magnetic transition window narrows. The switching between the presence and absence of hysteresis behavior, occurring at temperatures below T_N, indicates a transition in the microscopic spin

structure[41–44]. Therefore, the difference in the orientation of stripe domains and the disappearance of hysteresis suggest the presence of two distinct magnetic structures, with a phase transition occurring between 0.4 K and 4.0 K. The precise temperature-dependent measurements reveal the vanishing of hysteresis around 2.5 K, indicating the manifestation of a spin phase transition, while the second magnetic transition supports the same inference. The spin structure is expected to show more pronounced characteristics at the atomic scale, and potential coupling with electronic states may also be observed. Accordingly, we plot H-T phase diagram of $GdTi_3Bi_4$ by extracting the magnetic transition window and field hysteresis at various temperatures (Fig. 4e).

Repeatable observation of CDW in $GdTi_3Bi_4$

Except for the data shown in the main Figures, we have verified the existence of the CDW exhibiting the same periodicity and orientation with the crystalline lattice across different samples and tips from three different growth batches (Fig. S15).

Data availability

The main figure data generated in this study are provided in the Source Data file. Additional data measured or analyzed during this study are available from the corresponding authors upon request. Source data are provided with this paper.

References

1. Grüner, G. *Density Waves in Solids* (Addison-Wesley Pub. Co., Advanced Book Program, 1994).
2. Chen, C.-W., Choe, J. & Morosan, E. Charge density waves in strongly correlated electron systems. *Rep. Prog. Phys.* **79**, 084505 (2016).
3. Grüner, G. The dynamics of spin-density waves. *Rev. Mod. Phys.* **66**, 1–24 (1994).
4. Samarakoon, A. M. et al. Bootstrapped dimensional crossover of a spin density wave. *Phys. Rev. X* **13**, 041018 (2023).
5. Chen, H. & Gao, H.-J. Widespread pair density waves spark superconductor search. *Nature* **618**, 910–912 (2023).
6. Agterberg, D. F. et al. The physics of pair-density waves: cuprate superconductors and beyond. *Annu. Rev. Condens. Matter Phys.* **11**, 231–270 (2020).
7. Wu, P. et al. Unidirectional electron–phonon coupling in the nematic state of a kagome superconductor. *Nat. Phys.* **19**, 1143–1149 (2023).
8. Joe, Y. I. et al. Emergence of charge density wave domain walls above the superconducting dome in 1T-$TiSe_2$. *Nat. Phys.* **10**, 421–425 (2014).
9. Nie, L. et al. Charge-density-wave-driven electronic nematicity in a kagome superconductor. *Nature* **604**, 59–64 (2022).
10. Zhang, Z. et al. Nematicity and charge order in superoxygenated $La_{2-x}Sr_xCuO_{4+y}$. *Phys. Rev. Lett.* **121**, 067602 (2018).
11. Ishioka, J. et al. Chiral charge-density waves. *Phys. Rev. Lett.* **105**, 176401 (2010).
12. Song, X. et al. Atomic-scale visualization of chiral charge density wave superlattices and their reversible switching. *Nat. Commun.* **13**, 1843 (2022).
13. Jiang, Y.-X. et al. Unconventional chiral charge order in kagome superconductor KV_3Sb_5. *Nat. Mater.* **20**, 1353–1357 (2021).
14. Xing, Y. et al. Optical manipulation of the charge-density-wave state in RbV_3Sb_5. *Nature* **631**, 60–66 (2024).
15. Son, J. H., Hsu, Y.-T. & Kim, E.-A. Switching between superconductivity and current density waves in Bernal bilayer graphene. *Phys. Rev. B* **111**, 115144 (2025).
16. Slough, C. G., McNairy, W. W., Coleman, R. V., Drake, B. & Hansma, P. K. Charge-density waves studied with the use of a scanning tunneling microscope. *Phys. Rev. B* **34**, 994–1005 (1986).
17. Fert, A., Ramesh, R., Garcia, V., Casanova, F. & Bibes, M. Electrical control of magnetism by electric field and current-induced torques. *Rev. Mod. Phys.* **96**, 015005 (2024).
18. Jiang, K., Zhou, S. & Wang, Z. Textured electronic states of the triangular-lattice Hubbard model and Na_xCoO_2. *Phys. Rev. B* **90**, 165135 (2014).
19. Allred, J. M. et al. Double-Q spin-density wave in iron arsenide superconductors. *Nat. Phys.* **12**, 493–498 (2016).
20. Chen, K. et al. Evidence of spin density waves in $La_3Ni_2O_{7-\delta}$. *Phys. Rev. Lett* **132**, 256503 (2024).
21. Chen, Y. et al. Intertwined charge and spin density waves in a topological kagome material. *Phys. Rev. Res.* **6**, L032016 (2024).
22. Yu, S.-L. & Li, J.-X. Chiral superconducting phase and chiral spin-density-wave phase in a Hubbard model on the kagome lattice. *Phys. Rev. B* **85**, 144402 (2012).
23. Liu, Y. et al. Superconductivity under pressure in a chromium-based kagome metal. *Nature* **632**, 1032–1037 (2024).
24. Teng, X. et al. Discovery of charge density wave in a kagome lattice antiferromagnet. *Nature* **609**, 490–495 (2022).
25. Teng, X. et al. Magnetism and charge density wave order in kagome FeGe. *Nat. Phys.* **19**, 814–822 (2023).
26. Cheng, E. et al. Striped magnetization plateau and chirality-reversible anomalous Hall effect in a magnetic kagome metal. Preprint at https://doi.org/10.48550/arXiv.2409.01365 (2024).
27. Cheng, E. et al. Interwoven magnetic kagome metal overcomes geometric frustration. *Nat. Mater.* https://doi.org/10.1038/s41563-025-02414-4 (2025).
28. Zhang, R. et al. Observation of orbital-selective dual modulations in an anisotropic antiferromagnetic kagome metal $TbTi_3Bi_4$. *Phys. Rev. X* **15**, 031012 (2025).
29. Jiang, Z. et al. Topological surface states in quasi-two-dimensional magnetic kagome metal $EuTi_3Bi_4$. *Sci. Bull.* **69**, 3192–3196 (2024).
30. Park, P. et al. Spin density wave and van Hove singularity in the kagome metal $CeTi_3Bi_4$. *Nat. Commun.* **16**, 4384 (2025).
31. Ortiz, B. R. et al. Evolution of highly anisotropic magnetism in the titanium-based kagome metals $LnTi_3Bi_4$ (ln: La...Gd3+, Eu2+, Yb2+). *Chem. Mater.* **35**, 9756–9773 (2023).
32. Guo, J. et al. Tunable magnetism and band structure in kagome materials $RETi_3Bi_4$ family with weak interlayer interactions. *Sci. Bull.* **69**, 2660–2664 (2024).
33. Trontl, V. M. et al. Interplay of Kondo physics with incommensurate charge density waves in $CeTe_3$. Preprint at https://doi.org/10.48550/arXiv.2502.04814 (2025).
34. Gyenis, A. et al. Quasi-particle interference of heavy fermions in resonant X-ray scattering. *Sci. Adv.* **2**, e1601086 (2016).
35. Aishwarya, A. et al. Melting of the charge density wave by generation of pairs of topological defects in UTe_2. *Nat. Phys.* **20**, 964–969 (2024).
36. LaFleur, A. et al. Inhomogeneous high temperature melting and decoupling of charge density waves in spin-triplet superconductor UTe_2. *Nat. Commun.* **15**, 4456 (2024).
37. Guo, J. et al. Tunable bifurcation of magnetic anisotropy and bi-oriented antiferromagnetic order in kagome metal $GdTi_3Bi_4$. *Phys. Rev. Lett.* **134**, 226704 (2025).
38. Crivillero, M. V. A. et al. Surface and electronic structure at atomic length scales of the nonsymmorphic antiferromagnet $Eu_5In_2Sb_6$. *Phys. Rev. B* **106**, 035124 (2022).
39. Hu, Y. et al. Real-space observation of incommensurate spin density wave and coexisting charge density wave on Cr (001) surface. *Nat. Commun.* **13**, 445 (2022).
40. Lawler, M. J. et al. Intra-unit-cell electronic nematicity of the high-Tc copper-oxide pseudogap states. *Nature* **466**, 347–351 (2010).
41. Matsuura, K. et al. Low-temperature hysteresis broadening emerging from domain-wall creep dynamics in a two-phase competing system. *Commun. Mater.* **4**, 71 (2023).

42. Baranov, N. V. et al. Magnetic phase transitions, metastable states, and magnetic hysteresis in the antiferromagnetic compounds $Fe_{0.5}TiS_{2-y}Se_y$. *Phys. Rev. B* **100**, 024430 (2019).
43. Maat, S., Thiele, J.-U. & Fullerton, E. E. Temperature and field hysteresis of the antiferromagnetic-to-ferromagnetic phase transition in epitaxial FeRh films. *Phys. Rev. B* **72**, 214432 (2005).
44. Rikvold, P. A., Brown, G., Miyashita, S., Omand, C. & Nishino, M. Equilibrium, metastability, and hysteresis in a model spin-crossover material with nearest-neighbor antiferromagnetic-like and long-range ferromagnetic-like interactions. *Phys. Rev. B* **93**, 064109 (2016).

Acknowledgements

We thank W. Ji and J.-J. Zhang for helpful discussions. The work is supported by grants from the National Natural Science Foundation of China (62488201(H.-J.G.), 92580202 (H.C.), 12347107 (M.L., C.T., and H.Y.), 12522408(SYZ) and 12374199 (SYZ)), the National Key Research and Development Projects of China (2022YFA1204100 (H.-T.Y., H.C.), 2021YFA1400100 (H.Y.), 2025YFA1212800 (SYZ)), the CAS Project for Young Scientists in Basic Research (YSBR-003 (H.C.)), the New Cornerstone Science Foundation through the Xplorer Prize (H.Y.), and the China National Postdoctoral Program for Innovative Talents (BX20250172) (X.H.). B.Y. acknowledges the financial support by the Israel Science Foundation (ISF: 2932/21, 2974/23), German Research Foundation (DFG, CRC-183, A02), and by a research grant from the Estate of Gerald Alexander. Z.W. is supported by the US DOE, Basic Energy Sciences (Grant No. DE-FG02-99ER45747) and by Research Corporation for Science Advancement (Cottrell SEED award number 27856).

Author contributions

H.-J.G. and H.C. design the experiments. X.H., H.C., Z.C., and Y.S. performed the STM/S experiments. J.-W.G., F.F., R.W., Z.Z., H.-T.Y., and F.S. prepared the $GdTi_3Bi_4$ crystals and performed the transport experiments. J.-F.G., R.Z., and S.Z. perform the MFM measurements. Z.W. did the theoretical consideration. H.T., B.Y. did the DFT calculations, and C. T., M.-R.L., and H.Y. performed theoretical calculations. X.H., H.C., Z.W., and H.-J.G. wrote the manuscript with input from all other authors. H.-J.G. supervised the project.

Competing interests

The authors declare no competing interests.

Additional information

Supplementary information The online version contains supplementary material available at https://doi.org/10.1038/s41467-026-69544-4.

Correspondence and requests for materials should be addressed to Hui Chen, Shiyu Zhu, Ziqiang Wang or Hong-Jun Gao.

Peer review information *Nature Communications* thanks Tristan Cren and the other, anonymous, reviewer(s) for their contribution to the peer review of this work. A peer review file is available.